pubs.acs.org/ac

analytical chemistry

January 26, 2021 Volume 93 Number 3

ACS Publications
Most Trusted. Most Cited. Most Read.

www.acs.org

analytical chemistry

pubs.acs.org/ac Article

Concurrent Vibrational Circular Dichroism Measurements with Infrared Spectroscopic Imaging

Yamuna Phal, Kevin Yeh, and Rohit Bhargava*

Cite This: *Anal. Chem.* 2021, 93, 1294−1303 Read Online

ACCESS | Metrics & More | Article Recommendations | Supporting Information

ABSTRACT: Vibrational circular dichroism (VCD) spectroscopy has emerged as a powerful platform to quantify chirality, a vital biological property that performs a pivotal role in the metabolism of life organisms. With a photoelastic modulator (PEM) integrated into an infrared spectrometer, the differential response of a sample to the direction of circularly polarized light can be used to infer conformation handedness. However, these optical components inherently exhibit chromatic behavior and are typically optimized at discrete spectral frequencies. Advancements of discrete frequency infrared (DFIR) spectroscopic microscopes in spectral image quality and data throughput are promising for use toward analytical VCD measurements. Utilizing the PEM advantages incorporated into a custom-built QCL microscope, we demonstrate a point scanning VCD instrument capable of acquiring spectra rapidly across all fingerprint region wavelengths in transmission configuration. Moreover, for the first time, we also demonstrate the VCD imaging performance of our instrument for site-specific chirality mapping of biological tissue samples. This study offers some insight into future possibilities of examining small, localized changes in tissue that have major implications for systemic diseases and their progression, while also laying the groundwork for additional modeling and validation in advancing the capability of VCD spectroscopy and imaging.

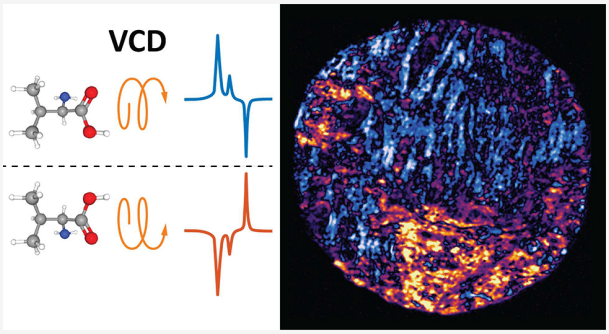

Chirality is an extrinsic geometric property, wherein the molecule forms a nonsuperimposable mirror image with its enantiomer. Such chiral pairs, also known as stereoisomers, are typically characterized as either right-handed or left-handed depending on the molecular structure. Many biomolecules essential for life are chiral, and one stereoisomer is typically more effective for specific biological processes. Further, in addition to chirality arising from structural arrangements, chirality of a molecule can also be conformational. The composition as well as structural and/or conformational chirality plays a dominant role in the efficacy and kinetics of the molecular interactions. Thus, understanding chirality is crucial to the entire discipline of biomedical sciences. While absorption of light in the mid-infrared (IR) spectral region provides information about the molecular composition of a sample, the differential absorption of left circularly polarized (LCP) and right circularly polarized (RCP) light provides an empirical way of quantifying its chirality. Specifically, vibrational circular dichroism (VCD) spectroscopy optically measures this difference in attenuation, providing an accurate and convenient analytical method to estimate chirality. Over the last two decades, the availability of density functional theory (DFT) models[1,2] and instrumentation[3−8] to compute and evaluate VCD spectra[9−13] has greatly furthered our scientific and analytical understanding of this concept. However, all experiments have largely been of homogeneous samples. Most often, these samples are aqueous solutions with measurements conducted in transmission mode.

Originally built around dispersive spectrometers, most current VCD instruments rely on interferometry, and the throughput and multiplex advantages of Fourier transform (FT) IR spectrometers.[14] Given the small signal, this technique typically requires relatively long acquisition times, typically ranging from 30 min[15] to several hours[16] or more, to collect sufficient coaverages and achieve a signal-to-noise ratio commensurate for analysis. In particular, quantitative estimates of fractional secondary structure content and site-specific information for biopolymers is still a significant challenge with FT-IR spectrometers for VCD analysis.[17] Additionally, broadband source-based FT-IR spectrometers have also been used for sample mapping and imaging. As light from the weak, broadband source is spatially distributed over a large area and the performance of multipixel detectors is considerably worse, imaging spectrometers show a reduction in signal-to-noise

Received: January 22, 2020
Accepted: November 30, 2020
Published: December 15, 2020

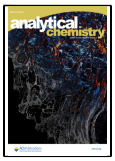

https://dx.doi.org/10.1021/acs.analchem.0c00323
Anal. Chem. 2021, 93, 1294−1303

ratio (SNR) compared to nonimaging spectrometers. Thus, while significant progress has been made in investigating dynamic molecular properties under stimuli or mixing, the mechanism of using FT-IR imaging to measure VCD has not been reported. The limited sensitivity of FT-IR imaging and the long acquisition times needed for VCD is a combination potentially impractical of acquiring reliable measurements. Recent advances in theory and design, however, have made high speed and high sensitivity IR imaging measurements possible.[18−26]

We propose to build on these recent advances in imaging, especially in using a custom-built quantum cascade laser (QCL)-equipped microscope,[27] to record VCD data in an imaging configuration. QCLs differ from traditional thermal FT-IR sources in several aspects. QCLs are intrinsically linearly polarized, which negates the need for an external polarizer and allows use of the extensive power of the source, thereby making them a superior choice for VCD measurements. Several attempts have been made to acquire VCD spectra using QCLs for a limited frequency range and for very small molecules in solution form.[28,29] Furthermore, rather than the weak, incoherent and diffuse radiance of an FT-IR globar source, QCLs have far higher intensities with a coherent beam that can be focused to a spot only microns wide. With such a focused detection volume, we introduce the option of generating a stereoisomer-specific chemical map of the sample based on its VCD response. We report VCD spectra acquisition for midsize molecules such as proteins with integration time of under ∼2 min and in solid form. Furthermore, we report VCD spectra in transmission sampling configuration to analyze spatially complex samples in their native state. We examine the differences in the theory, instrumentation, and acquisition methodologies, and report on the contrasts between the results from these configurations. Finally, we demonstrate rapid, spatially resolved VCD imaging, thus introducing a practical tool for investigation into the nature of chirality in biomedical samples.

DESIGN AND METHODOLOGY

QCL-VCD Spectroscopic Microscopy. A generalized layout of our QCL-VCD microscope is shown in Figure 1, demonstrating capabilities for spectroscopic imaging of samples in transmission configuration. The design builds upon a custom-built stage-scanning microscope design[27] that enables fast, point-by-point, high-definition image acquisition. We employ a continuously tunable QCL source (LaserTune, Block Engineering) with four multiplexed tuners that together emit an IR beam tunable between 770 and 1940 cm^{-1}, with a spectral line width of 2 cm^{-1}, and pulsed up to 2 MHz with a 6% duty cycle. Laser pointing is controlled by a pair of galvanometer mirrors (6215H, Cambridge Technology) that can be controlled to stabilize the pointing direction of laser beam. Next, we use a polarizer to further ensure a consistently polarized optical beam. The incident beam is focused using a chalcogenide glass (BD-2, $Ge_{28}Sb_{12}Se_{60}$) 0.71 numeric aperture (NA) refractive lens (OBJ_R) (#88−082, Edmund Optics) onto the sample. Out-of-focus scattered light is rejected by apertures (A) placed on the source and detection sides from the sample. Capability of transmission measurements is facilitated by incorporating a ZnSe broadband light optic (OBJ_T) with 0.71 NA and 12.7 mm EFL, and focusing the transmitted signal onto a cryogenic photovoltaic mercury cadmium telluride (PV MCT) detector (MCT-13-0.5PV,

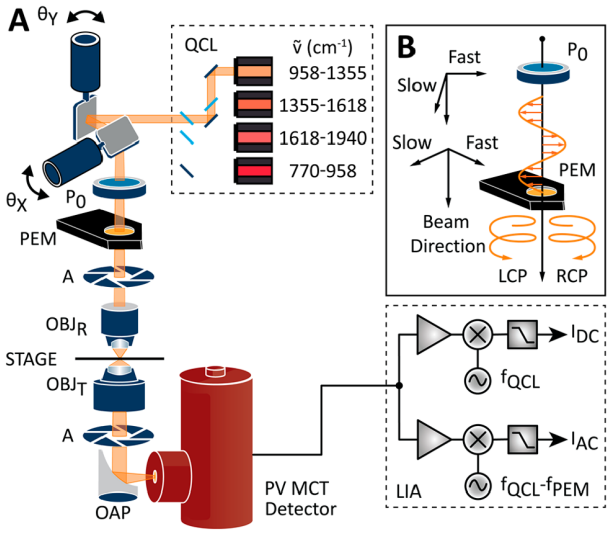

Figure 1. (A) Schematic of QCL-VCD microscope spanning the IR spectral fingerprint region with a PEM polarization control and lock-in detection at multiple demodulation frequencies, namely f_{QCL} and f_{QCL}-f_{PEM} that enable isolation of standard IR absorbance and VCD signals, respectively. (B) Inset plot shows the orientation of the fast axes of the polarizer (P_0) and PEM, and the resulting incident polarization states.

InfraRed Associates) using a 50.7 mm EFL reflective off-axis parabolic (OAP) mirror. The IR absorption spectrum is isolated by demodulating the signal at the laser modulation signal frequency using a lock-in amplifier (LIA) (MFLI, with F5M and MD, Zurich Instruments).

The QCL-VCD microscope setup acquires simultaneous IR and VCD images or spectra by using a second-generation digitally tunable photoelastic modulator (PEM) (PEM 200 IIZS50, Hinds Instruments). This device modulates the polarization of the transmitted optical beam based on the photoelastic effect, where voltage-controlled mechanical stress induces birefringence in the crystals that is proportional to the resulting strain. The PEM's fast optical axis is set to 45° with respect to the polarization direction of the incident IR beam and the maximum retardance is set corresponding to a design wavelength (λ_0), which is same as the QCL output beam wavelength. At the peak retardance of the PEM ($\lambda_0/4$), the result is a modulation between the LCP and RCP light states that oscillate sinusoidally at the PEM's resonant frequency (50 kHz). One of the major drawbacks of using a PEM with a highly coherent laser source such as the QCL is the complex and unpredictable fringe pattern produced by the superposition of coherent wavefronts internally reflected between the optical surfaces. To mitigate such undesirable interference effects and reflections, and eliminate any stray light occurring at an undesired peak retardation, the PEM is slightly tilted with respect to the optical beam, albeit keeping a 45° alignment between the fast optical axis and the direction of polarization. Additionally, antireflective coatings can facilitate improved performance through the reduced detrimental impacts arising from back and internal reflections.

Theoretical Background. The theoretical model of a FT-IR VCD spectrometer in standard transmission configuration is well-known.[2,7] We extend this formulation and provide a mathematical framework for a VCD system, using a coherent pulsed light source. The Stokes-Mueller formalism is a classic

https://dx.doi.org/10.1021/acs.analchem.0c00323
Anal. Chem. 2021, 93, 1294−1303

way[30] of characterizing an optical system by the mathematical representation of the response of each element in the optical train to excitation by polarized light. The polarization state of an optical beam is mathematically described as

$$\mathbf{S} = \begin{Bmatrix} I \\ Q \\ U \\ V \end{Bmatrix} = \begin{Bmatrix} I_T \\ I_{0^\circ} - I_{90^\circ} \\ I_{45^\circ} - I_{135^\circ} \\ I_R - I_L \end{Bmatrix} \quad (1)$$

where I is the total intensity and sum of all the orthogonal polarizations, Q and U are the differences in the linear polarization components, and V is the differential circular polarization component (RCP − LCP). The linear interaction of an optical device with a beam of light can be described as a transformation of an incident Stokes vector S_i into an emerging Stokes vector, $S_O = MS_i$, where M is the Mueller matrix that is characteristic of the optical device or system. Without any instrumental polarization, the matrix, M, equals the identity matrix and $S_O = S_i$. The transformation of an initial Stokes vector by a sequence of optical devices is given by the consecutive product of the matrices representing each element, including the rotation matrices due to the angles between their planes of incidence. The Mueller matrix representations for the various optical elements used in the setup are approximately described in eq 1, where any nonlinear effects, including the polarization change due to the lenses, are neglected. $S_0(f_{QCL}, \tilde{\nu})$ is the Stokes vector for the input QCL source beam, with pulse repetition rate f_{QCL} and peak intensity $I_0(\tilde{\nu})$ at wavenumber $\tilde{\nu}$. The individual Mueller matrices for the system can be represented sequentially with the sample, $M_X(\tilde{\nu})$, a low-emissivity slide approximated as an ideal mirror, $M_M(\tilde{\nu})$, a PEM, $M_{PEM}(f_{PEM}, \tilde{\nu})$, a polarizer, $M_P(\tilde{\nu})$, and a detector, $M_D(\tilde{\nu})$. The overall intensity is diminished by the absorbance factor of $10^{-A''(\tilde{\nu})}$. The total intensity recorded by the detector after passing through a train of optical elements can be expressed as

$$I_T(\tilde{\nu}) = M_D M_X(\tilde{\nu}) M_{PEM}(45^\circ, \alpha_M(\tilde{\nu})) M_P(0^\circ) S_0(f_{QCL}, \tilde{\nu})$$
$$= \frac{I_0(\tilde{\nu})}{4} 10^{-A''(\tilde{\nu})} (1 + 2J_1[\alpha_M^0(\tilde{\nu})] CD(\tilde{\nu}) + J_0[\alpha_M^0(\tilde{\nu})]) \quad (2)$$

where $J_0[\alpha_M^0(\tilde{\nu})]$ and $J_1[\alpha_M^0(\tilde{\nu})]$, are the zero and first order Bessel functions that are a function of the wavenumber and the peak PEM retardance angle specified by $\alpha_M^0(\tilde{\nu})$. Note that the PEM retardance angle varies sinusoidally as, $\alpha_M(\tilde{\nu}) = \alpha_M^0(\tilde{\nu}) \sin(2\pi f_{PEM} t)$. $J_1[\alpha_M^0(\tilde{\nu})]$ is associated with the transformation of the linearly polarized light into circular polarization, resulting in the first harmonic signal component. $J_0[\alpha_M^0(\tilde{\nu})]$ contributes to the fundamental signal component, and PEM phase is chosen such that $J_0[\alpha_M^0(\tilde{\nu})] = 0$. The standard transmission theory formulation can be specified by eq 3, where the acquired signal comprises of two dominant components, namely $\mathbf{I_{DC}}(\tilde{\nu})$ and $\mathbf{I_{AC}}(\tilde{\nu})$:

$$I_T(\tilde{\nu}) = \mathbf{I_{DC}}(f_{QCL}, \tilde{\nu}) + \mathbf{I_{AC}}(f_{QCL} \pm f_{PEM}, \tilde{\nu}) \quad (3)$$

By using the following derivation for the CD intensity

$$CD = \frac{1}{2}\ln(10)[A_L(\tilde{\nu}) - A_R(\tilde{\nu})] = 1.1513\Delta A_{VCD}(\tilde{\nu}) \quad (4)$$

with the ratio of the AC and DC terms

$$\frac{\mathbf{I_{AC}}(\tilde{\nu})}{\mathbf{I_{DC}}(\tilde{\nu})} = J_1[\alpha_M^0(\tilde{\nu})][1.1513\Delta A_{VCD}(\tilde{\nu})] \quad (5)$$

we can isolate the VCD spectrum ($\Delta A_{VCD}(\tilde{\nu})$) as follows:

$$\Delta A_{VCD}(\tilde{\nu}) = \frac{1}{1.1513 J_1[\alpha_M^0(\tilde{\nu})]} \left[\frac{\mathbf{I_{AC}}(\tilde{\nu})}{\mathbf{I_{DC}^0}(\tilde{\nu})}\right] \quad (6)$$

In addition, measurement of IR absorbance ($A_{IR}(\tilde{\nu})$) is provided by

$$A_{IR}(\tilde{\nu}) = -\log_{10}\left(\frac{\mathbf{I_{DC}}(\tilde{\nu})}{\mathbf{I_{DC}^0}(\tilde{\nu})}\right) \quad (7)$$

Data Acquisition and Post-Processing. Circular dichroism cannot be achieved by separately measuring the response of a sample when illuminated with either form of circularly polarized light. To obtain a VCD spectrum, the polarization of the optical beam is modulated between LCP and RCP states just prior to the sample. The recorded differential intensity between RCP and LCP signal is denoted by I_{AC}, which is the magnitude of the demodulated complex signal at the difference or sum frequency ($f_{QCL} \pm f_{PEM}$), where f_{PEM} is the PEM's resonant frequency. Likewise, the signal acquired at the QCL's pulse repetition rate (f_{QCL}) is denoted by I_{DC}. IR absorbance (A) is calculated as the negative log of I_{DC}, whereas I_{AC} is scaled by I_{DC} to derive the VCD signal, as described in eqs 8 and 9, using a phase-sensitive lock-in amplifier. Figure 2

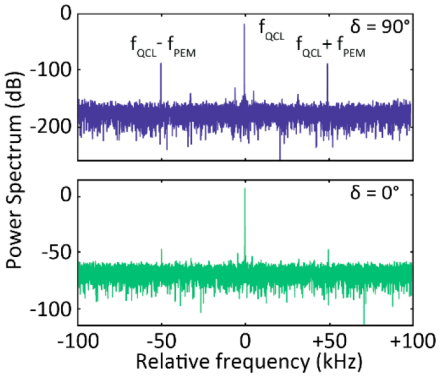

Figure 2. Power spectrum of the single beam IR signal and the corresponding demodulation frequencies for PEM retardance $\delta = 90°$ (top) and PEM retardance $\delta = 0°$ (bottom).

depicts the power spectrum of the acquired signal. For simplification purposes, let us substitute $\frac{\mathbf{I_{DC}}(\tilde{\nu})}{\mathbf{I_{DC}^0}(\tilde{\nu})} = I_{DC}$, and separately denote the sample and background intensities as I_S and I_{BG}, respectively, where $I_S(f_{QCL}) = \mathbf{I_{DC}}(f_{QCL}, \tilde{\nu})$ and $I_{BG}(f_{QCL}) = \mathbf{I_{DC}^0}(f_{QCL}, \tilde{\nu})$.

$$A = -\log_{10}\frac{I_S(f_{QCL})}{I_{BG}(f_{QCL})} = -\log_{10}(I_{DC}) \quad (8)$$

$$VCD = \frac{I_S(f_{QCL} \pm f_{PEM}) - I_{BG}(f_{QCL} \pm f_{PEM})}{I_S(f_{QCL})/I_{BG}(f_{QCL})} = \frac{I_{AC}}{I_{DC}} \quad (9)$$

https://dx.doi.org/10.1021/acs.analchem.0c00323
Anal. Chem. 2021, 93, 1294−1303

The IR absorption and VCD spectra thus acquired are background subtracted to correct for instrument effects such as scattering. The filter time constant and the noise bandwidth are important parameters that affect the SNR of any phase-sensitive detectors such as the LIA. Since this a weak process, we can improve the SNR by slowing the acquisition speed to adjust the integration time constants. The time constant is adjusted to provide an optimal balance of responsiveness and stability ($\tau = t_x/C$) and, in imaging mode, is set relative to the minimum pixel dwell time (t_x), scaled by a lock-in specific parameter (C). Depending on the low-pass filter order, the response time for the LIA measurement reaches a steady state value in its rated steady state multiple, denoted as C_T. By increasing the time constant, the noise in the output signal value is reduced, but with a consequent trade-off in system responsiveness and acquisition speed.

Having discussed the process of signal acquisition, next we discuss the essential data processing steps required to obtain the VCD spectra. A fifth-order low-pass filter with a settling time of approximately 3τ and a roll-off of 30 dB/oct is used. We acquire spectra spanning 1400−1800 cm^{-1} in 2 cm^{-1} steps. The acquisition time per wavenumber includes approximately 200 ms to tune and settle the laser, while also allowing for spectral tuning of the PEM, followed by 50 ms pixel dwell time, which amounts to ∼2 min in total per point spectrum. However, to ensure statistical repeatability and reproducibility of the acquired data, 20 consecutive measurements were acquired from each of 4 different pixels across the sample. For noise reduction, all VCD spectral data are processed using a fifth order polynomial Savitzky-Golay finite impulse response (FIR) smoothing filter with a frame length of 11. We use a piece-wise baseline correction algorithm to correct for amplitude variations in the spectra that are caused by light-sample interactions (dominantly, scattering) and instrument effects. Our system, with its improved SNR and reduced integration times, also enables us to map the VCD signal over the sample to form images. Instead of sweeping the spectra, we detect the signal locked to the specific frequency of interest,[31] by scanning the stage. Similar to VCD spectroscopy, the demodulated signal is obtained at the difference frequency and is used to form the image, as the stage scans the sample.

Sample Preparation. Various proteins exhibit chirality, including several commercially available model proteins, such as myoglobin, bovine serum albumin (BSA), cytochrome c, lysozyme, and concanavalin A. These representative proteins contain a variety of secondary structures with a range of optical activity − α-helix, a random mixture, and β-sheet, respectively. All samples were dissolved to a concentration of 300 mg/mL in H_2O solvent.[32−34] Concanavalin A was dissolved in 100 mM phosphate buffer with pH 6. The samples were drop cast (0.5 μL) on a polished plasma-cleaned 25 mm diameter, 2 mm thick BaF_2 substrate (Spectral Systems) and dried under normal air flow. In each case, the substrate was first cleaned with acetone and isopropyl alcohol (IPA) and then rinsed with distilled water. The plasma cleaning further removes any organic contaminants and helps increase the surface adhesion and hydrophilicity that enhances bonding between the window and the protein solutions, enabling the formation of very thin protein films.

RESULTS AND DISCUSSION

We have implemented VCD analysis in a DFIR imaging spectrometer, as depicted schematically in Figure 1. The system retains the imaging quality of an IR microscope and additionally provides a complementary capability for VCD measurements with an augmentation of a PEM in the design. First, we discuss the unique characteristics of this optical component and its effect on our measurements for imaging. The necessary generation of rapidly switching states of circularly polarized light in VCD spectrometers is enabled by PEM operation. By their implicit nature, waveplates, including PEMs, exhibit chromatic behavior and are typically optimized at discrete spectral frequencies. The differential transmission of the beam, centered at a fixed frequency in a PEM crystal, limits the PEM broadband operation since the fast axis orientation slightly varies with wavenumber. The absolute magnitude of this modulator chromatic variation over the entire operating wavenumber range varies between 10% to 20% of the nominal value, which can affect the generation of the circular polarization beam. This presents an obvious inefficiency for FT-IR spectrometers, where all wavenumbers are transmitted simultaneously, in only being effective over a limited bandwidth and not providing an equally high quality of polarization at all wavenumbers. Since the efficiency of the PEM is not consistent through the entire spectral frequency range, ideally, filters are also necessary to restrict the transmitted range when using a spectrally broadband source, and they further reduce both the throughput per se as well as the FT- multiplex advantage. The combination of reduced efficiency and light throughput caused by filters are severe disadvantages of an imaging configuration and, so far, have limited the use of FT-IR VCD spectroscopy in microscopic sample characterization.

Dispersive VCD instruments can gain in terms of component efficacy but cannot utilize the limited source intensity as efficiently; thus, both are limited for imaging. Since our implementation uses a discrete frequency, polarized, high intensity source, the drawbacks inherent in using PEMs for FT-IR imaging or a thermal source-based dispersive instrument for VCD can be avoided. The high intensity of the laser offsets the multiplex advantage of FT instruments and allows the retardance of the PEM to be changed in conjunction at the specified frequencies, eliminating the need for filters, reducing the need for calibrations or corrections, and condensing the problem to formulating meticulous synchronization strategies for accurate data acquisition. Moreover, calibration and baseline correction, which is a concern for FT-IR VCD spectroscopy, can also be avoided by locking into the specific sum or difference frequencies. Finally, the lock-in process also mitigates noise contributions due to stray light and any electrical offset in the detector circuitry. Since our proposed approach implements the optical train efficiently more so than conventional VCD instruments, it also allows for simplification of the optical design and enables leveraging of significant recent advances in IR microscopy. Interestingly, the conceptual, hardware, and measurement protocol of the proposed modality, provides advantages that combine the best of both FT and dispersive spectrometers. Together, these advantages might facilitate recording VCD data in a microscopy format.

Although the theoretical framework described earlier assumes a perfectly collimated and linearly polarized light source, real laser beams typically deviate from this ideal behavior. Hence, next, we characterize the polarization properties of the laser and discuss its implications on the performance of our QCL-VCD microscope. QCLs predominantly emit transverse magnetic (TM) polarized light with an

https://dx.doi.org/10.1021/acs.analchem.0c00323
Anal. Chem. 2021, 93, 1294−1303

electric field vector perpendicular to the plane of the quantum wells, which is characteristic of their fundamental structure. However, QCL emissions have also been reported to contain a small circular component and other orthogonal polarization components that could be attributed to the induced birefringence of the QCL waveguides used for directing the emitted light.[31] We experimentally verify the polarization characteristics of each laser in an example 4-laser QC system, with each laser tuned to the center wavenumber of its gain curve as shown in Figure 3A. A polarizer is placed in front of

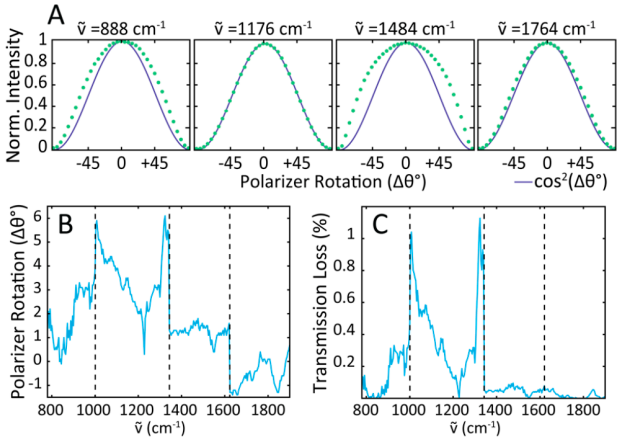

Figure 3. (A) Intensity variation for each of the center wavenumbers of an example 4-laser QC system, where the corresponding $\cos^2(\Delta\theta)$ fit shows that the emitted laser light is not purely linear. (B) The polarizer rotation angle ($\Delta\theta$) for maximum transmission varies with the wavenumber across the entire QCL spectrum range. (C) The corresponding transmission loss with polarizer orientation fixed at $\Delta\theta = 0°$ is less than 1% and depicted for the entire wavenumber range. Transitions between lasers are represented by the dashed lines.

the QCL such that the fast axis of the polarizer is aligned with the QCL's polarization axis. With the ideal assumption that the source polarization is purely vertical (corresponds to $\Delta\theta = 0°$), the orientation of the polarizer fast axis is varied with respect to the incident linear polarization such that the angle between them is $\Delta\theta$. We note that the detected intensity follows a $\cos^2(\Delta\theta°)$ variation. Even though the source polarization is not constant and varies across the wavenumber as shown in Figure 3B, the transmission loss is <1% (Figure 3C) with a fixed polarizer setup at $\Delta\theta = 0°$. Hence, a positionally static PEM is a valid assumption for our instrument. Lastly, we assume that the rest of the optical components have negligible polarizing effect on the system response.

One of the major applications of VCD spectral analysis has been in biopolymer structural studies. For globular proteins, the amide I and amide II vibrational modes' absorption features are widely used as a marker for relative conformational composition, due to their higher intensities and increased sensitivity to secondary structures compared to the amide III band. Hence, the analysis of VCD spectra in the mid-IR is traditionally limited to the spectral range 1400−1800 cm^{-1}.[35] Commonly, α-helical secondary structures are associated with 1650−1655 cm^{-1}. The IR band at 1633−1640 cm^{-1} is indicative of β-sheets, while an absorption between 1670−1690 cm^{-1} and a characteristic band around 1665 cm^{-1} is assigned to β-turns,[11,17,36,37] and random coil is usually associated with the IR band between 1640 and 1648 cm^{-1}.

We use representative proteins, namely, myoglobin, BSA, cytochrome c, lysozyme, and concanavalin A to validate our measurements. In Figure 4, in the first set, we compare the absorption spectra of the representative proteins in DFIR

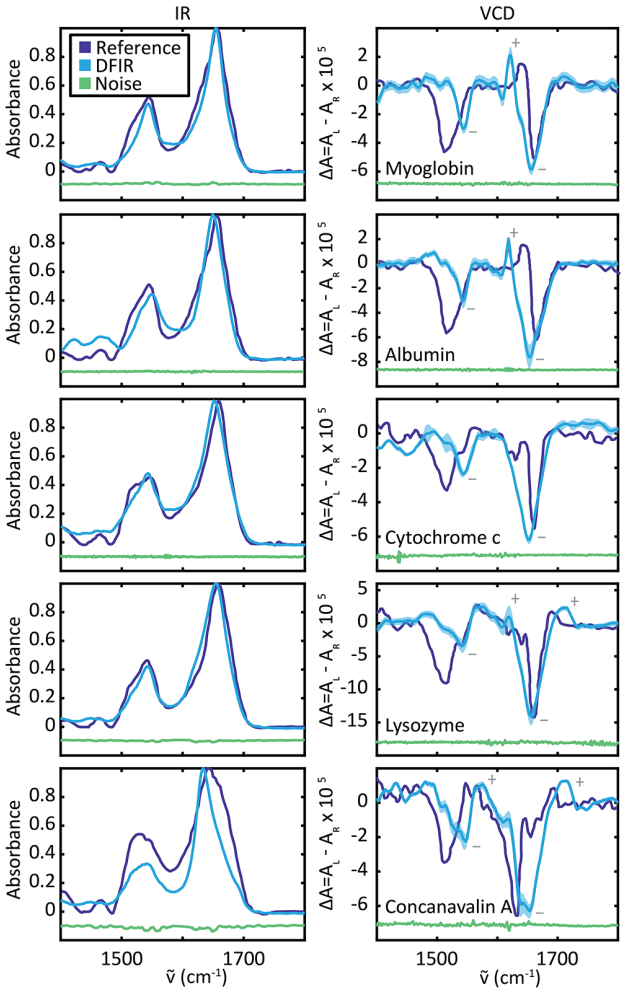

Figure 4. Fingerprint IR absorption spectra and the simultaneously acquired corresponding VCD spectra of five representative proteins: myoglobin, bovine serum albumin (BSA), cytochrome c, lysozyme, and concanavalin A between 1400 and 1800 cm^{-1} in transmission configuration. The noise spectra ordinate is offset and shown in the panel below each spectrum. The corresponding VCD spectra are obtained in transmission configuration and yield essentially comparable noise level, calculated as the standard deviation of 20 repeated measurements from each of the four different pixels across the sample. The $\pm 3\sigma$ standard deviation in the VCD spectra represents a 99.7% confidence level in the measurements. The characteristic signs of VCD spectra that are traditionally speculated to have the specific protein secondary structure are indicated with symbols ±. Also plotted are the reference FT-IR spectra for the same dried protein films but prepared in H_2O solution, except for β-sheets representative that was prepared in D_2O, which were reproduced with permission from a study described by Shanmugam, G.; Polavarapu, P. L. Vibrational circular dichroism of protein films. *J. Am. Chem. Soc.* **2004**, *126* (33), 10292−10295. Copyright 2004 ACS Publications. Note that myoglobin and concanavalin A VCD spectra for dried protein film samples are not available in the literature and are compared to the VCD spectra of another representative all-α protein, hemoglobin, and all-β protein, pepsin, respectively.

https://dx.doi.org/10.1021/acs.analchem.0c00323
Anal. Chem. 2021, 93, 1294−1303

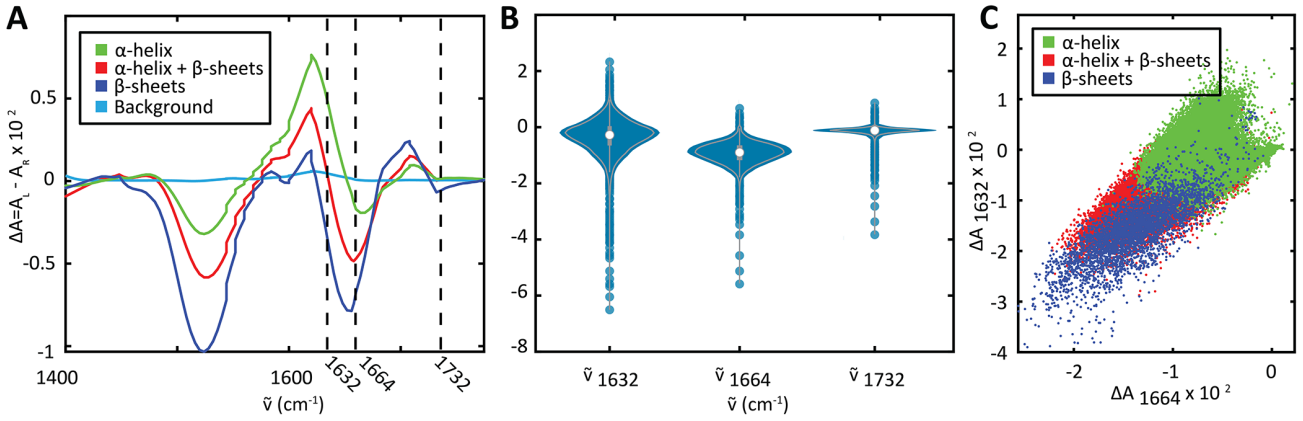

Figure 5. (A) k-means clustering of the hyperspectral data for a representative core, B12, shows four distinct spectra, with high resemblance to α-helix, β-sheets, a mixture, and lastly, the background. Three discrete wavenumbers, 1632, 1664, and 1732 cm^{-1}, which corespond to high data contrast, the contrast at amide I absorbance, and low data contrast, respectively, are marked with dashed lines. (B) Violin plots showing the underlying distribution of VCD intensity values for each non-background pixel in core B12 are shown. At 1632 cm^{-1}, the VCD signal shows a high contrast between the classes, with the data distribution being elongated. While the VCD signal shows a negative median at 1664 cm^{-1}, the distribution is tightly centered about the median at 1732 cm^{-1}. (C) Lastly, VCD values are plotted on the feature space corresponding to the 1664 cm^{-1} and 1632 cm^{-1} wavenumbers. A scatter plot of the clusters shows a clear distinction between the green and purple clusters, which have a high resemblance to the α-helical and β-sheet VCD signal in a native dried form.

configuration with the spectra obtained from the literature. The DFIR spectra acquired for the corresponding protein secondary structures show a high correlation with the FT-IR spectra and is in accordance with the Pearson statistics, with a significance value above 0.93. Further details on the correlation coefficient matrix and the values can be found in the Supporting Information (SI).

Next, we compare our recorded VCD spectra with those reported in other studies[10] using FT-IR spectroscopy. The average VCD spectra thus acquired is within three standard deviations, which accounts for about 99.7% confidence level, is as shown in Figure 4. The recorded spectra show that the secondary structures determine the dominant contributions to the VCD shape. A comparison of the VCD spectra demonstrates considerable similarities with respect to unique peak locations, yet there are also significant differences. The VCD spectra of proteins with dominant α-helix structures such as myoglobin (70%) and BSA have a characteristic $\pm$ couplet with zero-crossing at 1630 cm^{-1} in the amide I region. They also have a distinct intense negative VCD band in the amide II region as seen in Figure 4. Concanavalin A (45%) is a protein with dominant β-sheet structure. The amide I band shows a $\mp$ couplet and an intense negative band located at 1660 cm^{-1}, which is the typical signature of a β-sheet structure. It is exactly opposite to the characteristic signature of the α-helical structures in the amide I region. In the amide II region, a characteristic intense $\mp$ couplet is observed. Cytochrome c and lysozyme are proteins with α-helical (40%), β-turn (20%), and β-sheet structures. They show the characteristic $\pm$ couplet for helical structures with smaller intensity. However, due to the cancellation of the opposite bands in the amide I region, they are the most difficult to isolate. They also have a broader and less intense negative band in the amide II region. To summarize, the amide I region in all of the representative proteins show high correlation with FT-IR VCD spectra, with some frequency shifts in the positive lobe of amides I and II. Moreover, amide II shows a broad negative peak for α-helical structures such as myoglobin and is bisignate for β-sheet structures such as concanavalin A. These results confirm the association between FT-IR and DFIR VCD protein spectra. Moreover, for the proteins with a mix of helices and sheets, the positive shoulder at 1690 cm^{-1} could be indicative of some β-degree turn or antiparallel β-sheet structure. The VCD spectra generated on protein films is similar to the spectra generated in solution form.[38]

A comparison of both the main features in absorption spectra and consideration of noise in the VCD spectra (Figure 4) provide confidence that our data are consistent with the expectation of VCD from these molecules, under these sample preparation conditions and measurement optics. We especially note that the quality of the vibrational spectrum, as quantified previously,[19] is comparable to that commonly encountered in prior studies, demonstrating analytical utility. Thus, we show that VCD spectra can be recorded in a microscopy configuration in feasible times (each spectrum took ~2 min to acquire). To understand discrepancies in our spectra compared to those reported in the literature,[39] we examine experimental, theoretical, and instrumental limitations of our microscope. Foremost, we note that the VCD signal reported is comparable to that obtained in prior studies. Moreover, for the representative proteins shown, whose structures are relatively rigid, the expected VCD signal is an accurate manifestation of their chiroptical activity owing to their specific intra- and intermolecular interactions.[29] The location of the amide I and II bands is shifted with respect to that obtained by FT-IR spectrometer that could be a result of different conformational structures and sample preparation, sample volumes, equivalent path length, and sample thickness,[40] as well as due to optical effects associated with measuring samples in a microscope with condensing optics.[41] The net effect is an inhomogeneous broadening and change in line shape. An important consideration that encompasses both the experiment and the instrument is the calibration factor for VCD signal, which directly relates to the Bessel functions. Methods[5] that employ dual PEMs offer a systematic way of providing a baseline-corrected VCD spectra, without the need for a subsequent

https://dx.doi.org/10.1021/acs.analchem.0c00323
Anal. Chem. 2021, 93, 1294−1303

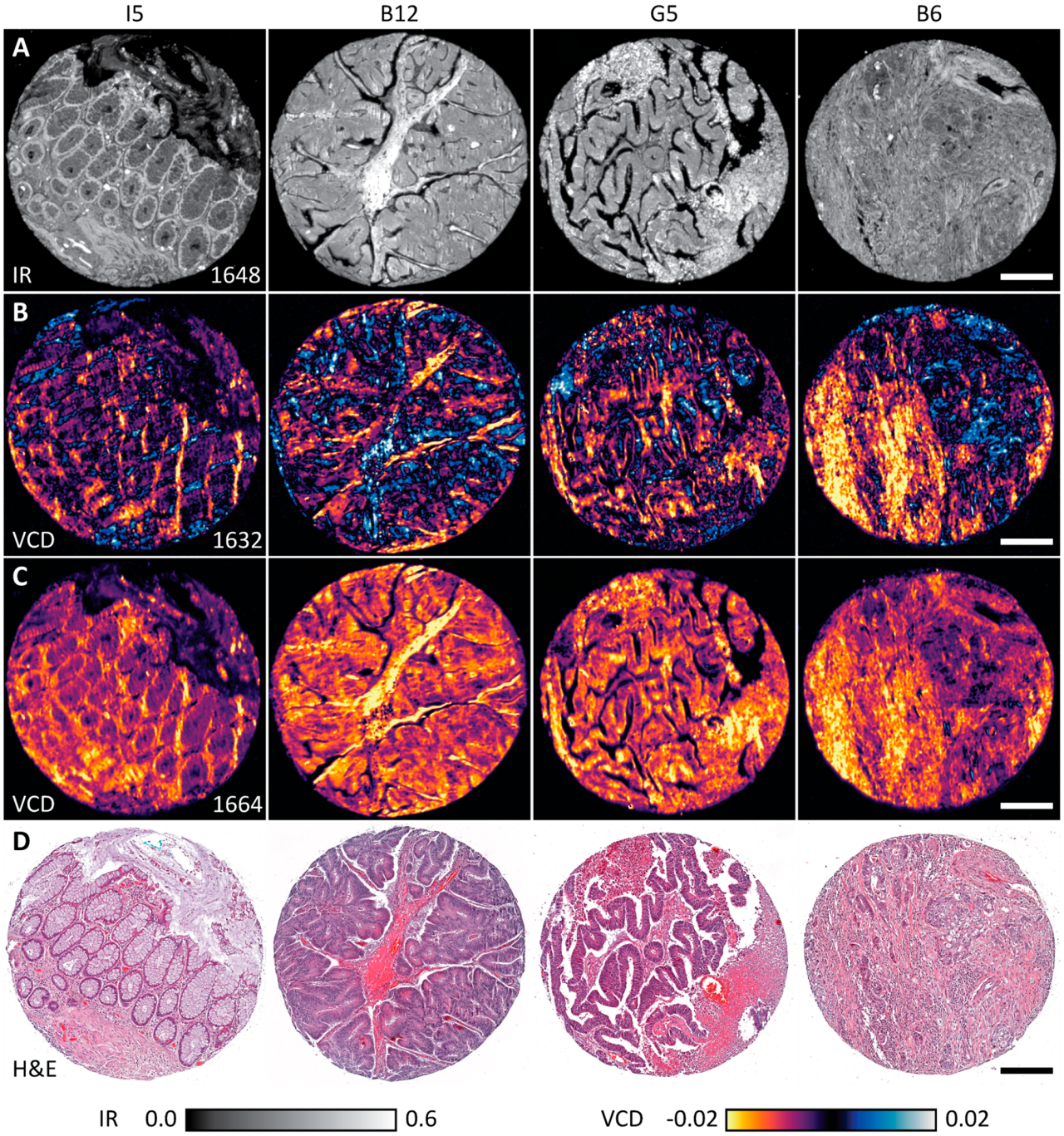

Figure 6. (A) Infrared amide I (1648 cm^{-1}) absorption, (B) 1632 cm^{-1} VCD, (C) 1664 cm^{-1} VCD, and (D) corresponding H&E-stained images of four samples from a TMA with normal (I5) and various grades of malignant (B12, G5, B6) colon tissue cores. The infrared absorbance and VCD data are acquired in transmission configuration. The alphabetic and numeric identifiers for each core corresponds to the row and column of the TMA, respectively. All scale bars are 250 μm.

VCD background measurement through the estimation of Bessel functions and the resulting product terms. Further development is required to incorporate these methods and improve the systematic calibration of the acquired spectra.

In addition to these known effects, the observed deviation could also be due to polarization. Discrepancies can arise from differential reflectivities of polarization states of the mirrors used in the beam path. Analysis of the polarization properties of QCL and the other optical elements is necessary, in terms of the individual Mueller matrix representations, which can better help understand the effects of polarized light on the optical system.[42,43] In principle, the nonideal instrumental polarization effects can be computed and compensated using standard contemporary modalities[44−46] that are well-known in the field of astronomy, for example. Many of these techniques can be implemented in future iterations of VCD microscopy systems. Regardless, the data demonstrates a clear need for further understanding and development of this technology. The initial

https://dx.doi.org/10.1021/acs.analchem.0c00323
Anal. Chem. 2021, 93, 1294−1303

demonstration that we report strongly reinforces the need for experimental refinement, greater theoretical understanding of VCD measurements in a microscopy configuration, and the need for extensive modeling to obtain quantitative measurements that can be rigorously validated with ab initio calculations.

Implementation of VCD in an IR microscope opens an exciting possibility of examining human tissues for chirality and their potential association with normal physiological functions or diseases. As a preliminary investigation to assess VCD images, we examine colon tissue samples in a configuration that is common in diagnostic pathology. To our knowledge, this is the first example of VCD data recorded in an IR imaging microscope. We demonstrate rapid pixel mapping to form hyperspectral absorption and VCD images of colon tissue with spectral steps of 4 cm^{-1}. In Figure 5, we illustrate the bands with highest VCD contrast. To identify the spectral bands that show the most significant VCD contrast, we use an unsupervised clustering technique followed by an estimation of the data distribution at each of these specified bands. We use k-means clustering to partition the pixelwise hyperspectral data set into predefined distinct nonoverlapping clusters that could be indicative of the secondary protein structures, namely, α-helix, β-sheets, a mixture, and lastly, the background. We estimate a k value of 4, which is an optimal number of data clusters for our given data set using silhouette analysis that determines the maximum possible degree of separation between clusters, while minimizing the distance from all data points in the same cluster. The algorithm follows an expectation-maximization problem such that the sum of the squared Euclidean distance between the data points within a cluster and its centroid is minimized. The average VCD spectra for each individual cluster are as shown in Figure 5A and they highly resemble the VCD spectra for α-helix, β-sheets, a mixture of the two proteins structures in their native form, and the background. Interestingly, the results from Figure 5A indicate that the characteristic frequencies exhibited by the specific conformations of the investigated protein secondary structures in native form highly correlates to corresponding conformations of globular proteins in the tissues. A positive VCD signal at 1632 cm^{-1} is indicative of an increased concentration of globular proteins with α-helices, whereas a negative VCD signal may suggest a higher presence of molecules with β-sheet structures. For biomolecules, which typically comprise of a mixture of α-helix and β-sheets, it is difficult to distinguish with only VCD signal at 1632 cm^{-1} as can be seen in Figure 5A, where the signal is near zero. Lastly, a spectral band such as 1732 cm^{-1} is a nonabsorbing wavenumber in VCD and shows approximately zero intensity for protein structures. As shown in Figure 5A, the VCD signal shows its maximum contrast with a transition from positive values to negative values at 1632 cm^{-1}, whereas the VCD intensity that corresponds to the amide-I absorbance shows a negative median at 1664 cm^{-1} and is centered at zero at 1732 cm^{-1}.

Next, in order to visualize the data distribution at each of these discrete wavenumbers of interest, we present the pixelwise data excluding the background, in the form of violin plots, such that the histogram at each wavenumber shows the estimated kernel density of the data at a specific VCD intensity value. From Figure 5B, the kernel distribution for wavenumber 1632 cm^{-1} is centered at zero, with a significant variance around the median values. Thus, a nonbackground pixel has a higher probability of showing a VCD intensity value around zero, with equal probabilities of showing positive or negative values. We can also predict from the wider width of the distribution around the median that most of the pixels have a mixture of protein secondary structures, with some possibility of β-sheets, although very less likely. Second, the data distribution for 1664 cm^{-1}, with a negative median value, shows less variance compared to that of 1632 cm^{-1}. Lastly, the predicted kernel distribution at 1732 cm^{-1} shows a comparatively narrower distribution, implying a mean value that equals the median. We go one step further to validate our clustering predictions. As shown in Figure 5C, the scatter plots of the clusters showing strong VCD contrast imply a clear separation between the green and purple clusters, which show significant resemblance to the α-helix and β-sheets, respectively. The wavenumbers, 1632 and 1664 cm^{-1}, which have the maximum variance in the VCD spectra are shown in the Figure 6B and 6C, respectively. A comparison of the amide-I absorbance image at 1648 cm^{-1} in Figure 6A and the respective VCD image at 1632 cm^{-1} shows interesting differences, with a positive VCD signal for some regions and a strong negative signal for others. The strong positive VCD signal denotes underlying α-helical secondary protein structures whereas a negative VCD signal shows a high correlation with the β-sheet structures, and an almost zero signal an indicative of a mixture or background. However, the VCD signal at 1664 cm^{-1} is intrinsically negative for all the three structures, which is indicative that proteins in biological tissue sections such as colon are homochiral. The pixel-wise collected data provides an image of the molecular and conformational structures as shown in Figure 6B,C, respectively. The SNR of these measurements is sufficient to realize important features in the tissue without the use of stains or dyes. Techniques, such as stainless staining[47] or classification can help identify important cell types and other conspicuous features in these tissues from absorption data as described in many studies.[48−54] We note, however, that the VCD data from tissues is unique and does not simply conform to absorption contrast in tissue. While the origins of VCD contrast and its utility will require an extended study, the development of the instrumentation described provides analytical capability to undertake such studies for colon and other tissue sections. As known during the development of FT-IR VCD instrument design, the lower intensity levels associated with VCD that typically range four to six orders below the absorbance signal magnitude are inherently difficult to isolate. Optical elements in the beam path and their relative alignment result in biases in the VCD signals that could show spectral as well as spatial dependence. Also, since the PEM is set such that the retardance sinusoidally varies to generate varying polarization states of the output beam, there could be a small contribution from the differential intensity in linear polarization states that could be reflected as a VCD signal. The other artifacts could also be due to the differential reflection or transmission at the optical surfaces that are present in the beam path as well as the differential response of the detector to the orthogonal polarization states. Regardless, this study presents the development of new tools that may improve our understanding of chirality in biomolecules and tissue samples. Local changes in any specific cellular or acellular tissue regions can now be explored. The ability to record data from small pixels and sample volumes is likely to be very useful in the study of pathologies that involve minute deposits of conformationally

https://dx.doi.org/10.1021/acs.analchem.0c00323
Anal. Chem. 2021, 93, 1294−1303

different proteins, as for example in Alzheimers disease.[55,56] This work not only paves the way for studies of chirality in tissue but also strengthens our analytical capability in examining small, localized changes in tissue that have major implications for systemic diseases.

CONCLUSIONS

We report a novel measurement technique of assessing VCD in an IR microscopic modality. Our instrument allows us to acquire VCD spectra in transmission configuration using a QCL-equipped stage-scanning DFIR microscope. We are able to measure site-specific VCD spectra of small volume midsize biomolecules (proteins) within a fraction of the time compared to a standard FT-IR VCD spectrometer. The ability to acquire measurements from small volumes in a microscopy configuration opens the innovative possibility of VCD imaging. Preliminary analysis of chirality in tissue suggests interesting features that could enable advances in the study of tissue structure toward the mechanisms of development and progression of diseases. Further methodical investigation is needed into the theory, modeling, and simulation of the data acquisition process, as there are many new directions that are now apparent. Together, this study is an important step in advancing practical VCD measurements with extended capabilities in a spectroscopic imaging configuration.

ASSOCIATED CONTENT

Supporting Information

The Supporting Information is available free of charge at https://pubs.acs.org/doi/10.1021/acs.analchem.0c00323.

Correlation coefficient matrix and the corresponding heat map for absorbance spectra of the representative proteins included (PDF)

AUTHOR INFORMATION

Corresponding Author

Rohit Bhargava − *Department of Electrical and Computer Engineering, Departments of Bioengineering, Mechanical Science and Engineering, Chemical and Biomolecular Engineering, and Chemistry, Cancer Center at Illinois, and Beckman Institute for Advanced Science and Technology, University of Illinois at Urbana−Champaign, Urbana, Illinois 61801, United States;* orcid.org/0000-0001-7360-994X; Email: rxb@illinois.edu

Authors

Yamuna Phal − *Department of Electrical and Computer Engineering and Beckman Institute for Advanced Science and Technology, University of Illinois at Urbana−Champaign, Urbana, Illinois 61801, United States*

Kevin Yeh − *Beckman Institute for Advanced Science and Technology, University of Illinois at Urbana−Champaign, Urbana, Illinois 61801, United States*

Complete contact information is available at: https://pubs.acs.org/10.1021/acs.analchem.0c00323

Notes

The authors declare the following competing financial interest(s): The University of Illinois has filed a provisional patent related to the described study on which all authors are named inventors.

ACKNOWLEDGMENTS

The authors thank Hyukjin Jang for help with sample preparation and appreciate useful discussions with Seth Kenkel and Sudipta Mukherjee. This work was supported in part by the National Institutes of Health via Grant No. R01EB009745 and the Cancer Center at Illinois.

REFERENCES

(1) Stephens, P. J.; Devlin, F. J. *Chirality* **2000**, *12* (4), 172−179.
(2) Stephens, P. J. *J. Phys. Chem.* **1985**, *89* (5), 748−752.
(3) Hilario, J.; Drapcho, D.; Curbelo, R.; Keiderling, T. A. *Appl. Spectrosc.* **2001**, *55* (11), 1435−1447.
(4) Dukor, R. K.; Nafie, L. A. Vibrational Optical Activity of Pharmaceuticals and Biomolecules. In *Encyclopedia of Analytical Chemistry*; John Wiley & Sons, Ltd.: Chichester, U.K., 2000; pp 1−15.
(5) Nafie, L. A. *Dual Polarization Modulation : A Real-Time, Spectral-Multiplex Separation of Circular Dichroism from Linear Birefringence Spectral Intensities*. 2000, *54* (11).
(6) Nafie, L. A. *Nat. Prod. Commun.* **2008**, *3* (3), 451−466.
(7) Nafie, L. A. *Vibrational Optical Activity*; John Wiley & Sons, Ltd.: Chichester, U.K., 2011; Vol. *492*.
(8) Keiderling, T. A. *Molecules* **2018**, *23* (9), 2404.
(9) Nafie, L. A.; Diem, M.; Vidrine, D. W. *J. Am. Chem. Soc.* **1979**, *101* (2), 496−498.
(10) Shanmugam, G.; Polavarapu, P. L. *J. Am. Chem. Soc.* **2004**, *126* (33), 10292−10295.
(11) Keiderling, T. A. *Chem. Rev.* **2020**, *120* (7), 3381−3419.
(12) Keiderling, T. A. *Curr. Opin. Chem. Biol.* **2002**, *6* (5), 682−688.
(13) Stephens, P. J.; Devlin, F. J.; Pan, J. J. *Chirality* **2008**, *20*, 643−663.
(14) Nafie, L. A.; Diem, M.; Vidrine, D. W. *J. Am. Chem. Soc.* **1979**, *101* (2), 496−498.
(15) Nafie, L. A.; Buijs, H.; Rilling, A.; Cao, X.; Dukor, R. K. *Appl. Spectrosc.* **2004**, *58* (6), 647−654.
(16) Polavarapu, P. L.; He, J. *Anal. Chem.* **2004**, *76* (3), 61A−67A.
(17) Keiderling, T. A.; Lakhani, A. Conformational Studies of Biopolymers, Peptides, Proteins, and Nucleic Acids. A Role for Vibrational Circular Dichroism. In *Comprehensive Chiroptical Spectroscopy*; John Wiley & Sons, Inc.: Hoboken, NJ, 2012; Vol. *56*, pp 707−758.
(18) Kole, M. R.; Reddy, R. K.; Schulmerich, M. V.; Gelber, M. K.; Bhargava, R. *Anal. Chem.* **2012**, *84* (23), 10366−10372.
(19) Mittal, S.; Yeh, K.; Leslie, L. S.; Kenkel, S.; Kajdacsy-Balla, A.; Bhargava, R. *Proc. Natl. Acad. Sci. U. S. A.* **2018**, *115* (25), E5651−E5660.
(20) Yeh, K.; Kenkel, S.; Liu, J.-N.; Bhargava, R. *Anal. Chem.* **2015**, *87* (1), 485−493.
(21) Guo, B.; Wang, Y.; Peng, C.; Luo, G. P.; Le, H. Q. *Appl. Spectrosc.* **2003**, *57* (7), 811−822.
(22) Bassan, P.; Weida, M. J.; Rowlette, J.; Gardner, P. *Analyst* **2014**, *139* (16), 3856−3859.
(23) Kröger, N.; Egl, A.; Engel, M.; Gretz, N.; Haase, K.; Herpich, I.; Kränzlin, B.; Neudecker, S.; Pucci, A.; Schönhals, A.; et al. *J. Biomed. Opt.* **2014**, *19* (11), 111607.
(24) Kuepper, C.; Kallenbach-Thieltges, A.; Juette, H.; Tannapfel, A.; Großerueschkamp, F.; Gerwert, K. *Sci. Rep.* **2018**, *8* (1), 7717.
(25) Ran, S.; Berisha, S.; Mankar, R.; Shih, W.-C.; Mayerich, D. *Biomed. Opt. Express* **2018**, *9* (2), 832.
(26) Tiwari, S.; Raman, J.; Reddy, V.; Ghetler, A.; Tella, R. P.; Han, Y.; Moon, C. R.; Hoke, C. D.; Bhargava, R. *Anal. Chem.* **2016**, *88* (20), 10183−10190.
(27) Yeh, K.; Lee, D.; Bhargava, R. *Anal. Chem.* **2019**, *91* (3), 2177−2185.
(28) Lüdeke, S.; Pfeifer, M.; Fischer, P. *J. Am. Chem. Soc.* **2011**, *133* (15), 5704−5707.
(29) Pfeifer, M.; Lüdeke, S.; Fischer, P. *Proc. SPIE* **2012**, *8219*, 821906.

(30) Goldstein, D. H. *Polarized Light, revised and expanded*; CRC press, 2003; ch. 3/5.
(31) Janassek, P.; Hartmann, S.; Molitor, A.; Michel, F.; Elsäßer, W. *Opt. Lett.* **2016**, *41* (2), 305.
(32) Baumruk, V.; Keiderling, T. A. *J. Am. Chem. Soc.* **1993**, *115* (15), 6939−6942.
(33) Baumruk, V.; Pancoska, P.; Keiderling, T. A. *J. Mol. Biol.* **1996**, *259* (4), 774−791.
(34) Urbanova, M.; Pancoska, P.; Dukor, R. K.; Gupta, V. P.; Keiderling, T. A. *Biochemistry* **1991**, *30* (43), 10479−10485.
(35) Ma, S.; Freedman, T. B.; Dukor, R. K.; Nafie, L. A. *Appl. Spectrosc.* **2010**, *64* (6), 615−626.
(36) Kong, J.; Yu, S. *Acta Biochim. Biophys. Sin.* **2007**, *39*, 549−559.
(37) Krimm, B. S.; Bandekar, J. *Vibrational spectroscopy and conformation of peptides, polypeptides, and proteins*, 1986.
(38) Shanmugam, G.; Polavarapu, P. L. *Appl. Spectrosc.* **2005**, *59* (5), 673−681.
(39) Kessler, J.; Andrushchenko, V.; Kapitan, J.; Bour, P. *Phys. Chem. Chem. Phys.* **2018**, *20*, 4926−4935.
(40) Lu, X.; Li, H.; Nafie, J. W.; Pazderka, T.; Pazderková, M.; Dukor, R. K.; Nafie, L. A. *Appl. Spectrosc.* **2017**, *71* (6), 1117−1126.
(41) Mayerich, D.; van Dijk, T.; Walsh, M. J.; Schulmerich, M. V.; Carney, P. S.; Bhargava, R. *Analyst* **2014**, *139* (16), 4031−4036.
(42) Berry, H. G.; Gabrielse, G.; Livingston, A. E. *Appl. Opt.* **1977**, *16* (12), 3200.
(43) Schaefer, B.; Collett, E.; Smyth, R.; Barrett, D.; Fraher, B.; Schaefer, B.; Collett, E.; Smyth, R.; Barrett, D.; Fraher, B. Measuring the Stokes Polarization Parameters. **2017**, *163* (2007).
(44) Tinbergen, J. *Publ. Astron. Soc. Pac.* **2007**, *119* (862), 1371−1384.
(45) Norris, B.; Schworer, G.; Tuthill, P.; Jovanovic, N.; Guyon, O.; Stewart, P.; Martinache, F. *Mon. Not. R. Astron. Soc.* **2015**, *14*, 1−14.
(46) Jäger, F. *Sol. Phys.* **1972**, *27*, 481−488.
(47) Mayerich, D.; Walsh, M. J.; Kadjacsy-Balla, A.; Ray, P. S.; Hewitt, S. M.; Bhargava, R. *Technology* **2015**, *03* (1), 27−31.
(48) Argov, S.; Ramesh, J.; Salman, A.; Sinelnikov, I.; Goldstein, J.; Guterman, H.; Mordechai, S. *J. Biomed. Opt.* **2002**, *7* (2), 248.
(49) Salman, A.; Argov, S.; Ramesh, J.; Goldstein, J.; Sinelnikov, I.; Guterman, H.; Mordechai, S. *Cell. Mol. Biol. (Noisy-le-grand).* **2001**, *47* (19), 159−166.
(50) Lasch, P.; Haensch, W.; Naumann, D.; Diem, M. *Biochim. Biophys. Acta, Mol. Basis Dis.* **2004**, *1688* (2), 176−186.
(51) Lasch, P.; Waesche, W.; McCarthy, W. J.; Mueller, G. J.; Naumann, D. *Proc. SPIE* **1998**, *3257*, 187−198.
(52) Travo, A.; Piot, O.; Wolthuis, R.; Gobinet, C.; Manfait, M.; Bara, J.; Forgue-Lafitte, M. E.; Jeannesson, P. *Histopathology* **2010**, *56* (7), 921−931.
(53) Beljebbar, A.; Bouché, O.; Diébold, M. D.; Guillou, P. J.; Palot, J. P.; Eudes, D.; Manfait, M. *Crit. Rev. Oncol. Hematol.* **2009**, *72* (3), 255−264.
(54) Nallala, J.; Lloyd, G. R.; Hermes, M.; Shepherd, N.; Stone, N. *Vib. Spectrosc.* **2017**, *91*, 83−91.
(55) Jucker, M.; Walker, L. C. Pathogenic Protein Seeding in Alzheimer Disease and Other Neurodegenerative Disorders; 2011.
(56) Soto, C.; Pritzkow, S. *Nat. Neurosci.* **2018**, *21*, 1332.

https://dx.doi.org/10.1021/acs.analchem.0c00323
Anal. Chem. 2021, 93, 1294−1303